Subduction earthquakes controlled by incoming plate geometry: The 2020 M>7.5 Shumagin, Alaska, earthquake doublet

Yu Jiang[a], Pablo J. González[a,b], Roland Bürgmann[c]

[a]*COMET, Department of Earth, Ocean and Ecological Sciences, School of Environmental Sciences, University of Liverpool, Liverpool, L69 3BX, United Kingdom,* Yu.Jiang@liverpoolac.uk

[b]*Volcanology Research Group, Department of Life and Earth Sciences, Instituto de Productos Naturales y Agrobiologıa (IPNA-CSIC), 38206 La Laguna, Tenerife, Canary Islands, Spain*, pabloj.gonzalez@csic.es

[c]*Department of Earth and Planetary Science, University of California, Berkeley, CA, USA,* burgmann@seismo.berkeley.edu

---

Subduction earthquakes controlled by incoming plate geometry: The 2020 M>7.5 Shumagin, Alaska, earthquake doublet

Yu Jiang[a], Pablo J. González[a,b], Roland Bürgmann[c]

[a] *COMET, Department of Earth, Ocean and Ecological Sciences, School of Environmental Sciences, University of Liverpool, Liverpool, L69 3BX, United Kingdom*
[b] *Department of Life and Earth Sciences, Instituto de Productos Naturales y Agrobiología (IPNA-CSIC), 38206 La Laguna, Tenerife, Canary Islands, Spain*
[c] *Department of Earth and Planetary Science, University of California, Berkeley, CA, USA*

Abstract

In 2020, an earthquake doublet, a M7.8 on July 22nd and a M7.6 on October 19th, struck the Alaska-Aleutian subduction zone beneath the Shumagin Islands. This is the first documented earthquake doublet involving a megathrust event and a strike-slip event. The first event partially ruptured a seismic gap, which has not hosted large earthquakes since 1917, and the second event was unusual as it broke a trench-perpendicular fault within the incoming oceanic slab. We used an improved Bayesian geodetic inversion method to estimate the fault slip distributions of the major earthquakes using Interferometric Synthetic Aperture Radar (InSAR) wrapped phase and Global Navigation Satellite Systems (GNSS) offsets data. The geodetic inversions reveal that the Shumagin seismic gap is multi-segmented, and the M7.8 earthquake ruptured the eastern segment from 14 km down to 44 km depth. The coseismic slip occurred along a more steeply, 26° dipping segment, and was bounded up-dip by a bend of the megathrust interface to a shallower 8°

dip angle connecting to the trench. The model for the M7.6 event tightly constrained the rupture depth extent to 19-39 km, within the depth range of the M7.8 coseismic rupture area. We find that the M7.6 event ruptured the incoming slab across its full seismogenic thickness, potentially reactivating subducted Kula-Resurrection seafloor-spreading ridge structures. Coulomb stress transfer models suggest that coseismic and/or postseismic slip of the M7.8 event could have triggered the M7.6 event. We conclude that the segmented megathrust structure and the location of intraslab fault structures limited the rupture dimensions of the M7.8 event and are responsible for the segmentation of the Shumagin seismic gap. Our study suggests that the western and shallower up-dip segments of the seismic gap did not fail and remain potential seismic and tsunami hazard sources. The unusual earthquake doublet provides a unique opportunity to improve our understanding of the role of the subducting lithosphere structure in the segmentation of subduction zones.

Keywords: Subduction earthquake doublet, slab geometry, Shumagin seismic gap, Alaska subduction zone

1. Introduction

In 2020, a pair of large and similar sized earthquakes (doublet) occurred along the eastern Aleutian subduction zone off the Alaska Peninsula (Fig. 1(a)). The first and largest earthquake of the doublet, with a moment magnitude (M_w) of 7.8, occurred at 06:12:44 UTC (22:12:44 local) on July 22 2020. On Oct 19 2020 at 20:54:39 UTC (12:54:39 local), an anomalously large aftershock (M_w=7.6) occurred 80 km southwest of the first event. According to the USGS catalog (https://earthquake.usgs.gov/earthquakes/eventpage/us7000asvb/executive, https://earthquake.usgs.gov/earthquakes/eventpage/us6000c9hg/executive), both earthquakes are located on the landward side of the subduction trench. The aftershocks of the first event are distributed parallel to the trench, while those of the second event are aligned perpendicular to the trench. The focal mechanism solutions from the GCMT catalog suggest the mechanism of the M7.8 event is of thrust-faulting type, while the M7.6 event was a strike-slip event. The centroid depths of both earthquakes were estimated as about 30-35 km. This suggests that the M7.8 event ruptured the buried megathrust interface, but the M7.6 event was caused by an unusual strike-slip rupture along an approximately trench-normal fault.

The 2020 Shumagin earthquake sequence is interesting for several reasons. Firstly, the mainshock is located within the Shumagin seismic gap. This portion of the subduction megathrust has been identified as a seismic gap since the 1970s (Sykes, 1971, Davies et al., 1981). The seismic gap stretches ~200 km along the Shumagin Islands and is bounded to the west by the 1946 M_w8.6 earthquake (López and Okal, 2006) and to the east by the 1938 M_w8.2 rupture (Freymueller et al., 2021). The last earthquakes that are inferred to have ruptured through part of or the whole Shumagin gap occurred in 1917, 1788, and possibly 1847 (Estabrook et al., 1994). If the whole Shumagin gap were fully locked at 5-32 km depth, the accumulated moment equates to 6.6×10^{19} Nm/year, assuming a plate convergence rate of 64 mm/year and a uniform rigidity of 50 GPa. This would require a M7.5 event every 4 years, or a M8 event every 20 years. The lack of historic M7.5+ earthquakes in the

Shumagin region has been explained due to substantial aseismic fault creep at seismogenic depths revealed by model inversions of inter-seismic GNSS velocities (Fournier and Freymueller, 2007). Fournier and Freymueller (2007) suggested that instead of rupturing in large earthquakes, most of the seismic moment in the Shumagin gap is released through steady creep, and a moderate M7 earthquake every $\sim$40 years, as observed in the last century, may be sufficient to accommodate the residual slip deficit. To the west of the Shumagin gap, a recent interseismic coupling model shows that the shallow portion along the Sanak segment, 240 km-long and 115 km-wide, might be partially locked, with 15%-25% coupling (Drooff and Freymueller, 2021). For the shallow portion along the Sanak segment, if the estimated 1946 earthquake rupture area, 180 km-long and 115 km-wide (López and Okal, 2006), was fully locked, and the remaining area is 20% coupled, the seismic moment deficit would be accumulating at around 4.5×10^{18} Nm/year. This calculation suggests that the seismic moment of the 1946 earthquake, 8.5×10^{21} Nm (López and Okal, 2006), released 1900 years of elastic strain accumulation along the Sanak segment. Large uncertainties are associated with estimating earthquake recurrence intervals, including the poorly constrained estimation of the 1946 earthquake slip and the assumption of the highest slip deficit near the trench in the interseismic coupling model (Drooff and Freymueller, 2021). Nevertheless, such long recurrence intervals could be the reason for there only being one documented major earthquake in the Sanak segment since 1700.

Secondly, the M7.6 slab-breaking aftershock had an unusual strike-slip mechanism and was deeply buried. Large oceanic lithosphere strike-slip events have previously occurred in the oceanic plate off subduction zones, such as the 2018 M_w7.9 Gulf of Alaska earthquake (Krabbenhoeft et al., 2018) and the 2012 M_w8.6 Wharton basin earthquakes off-Sumatra (Wei et al., 2013). Deep buried subduction earthquakes also can occur on reactivated fracture zones (Abercrombie et al., 2003, Lange et al., 2010). In addition, the subduction zone outer-rise region regularly hosts normal-faulting mechanisms events. Outer-rise normal-faulting events are attributed to plate bending stresses from slab pull, and can be modulated by the interplate seismic cycle (Kanamori, 1971). However, the occurrence of a major intraplate earthquake in the oceanic lithosphere just landward of the trench is rare, with only few reported examples, such as the October 4, 1994 M_w8.2 earthquake off Shikotan Island along the Kuril trench (Tanioka et al., 1995). Another notable example was a M_w7 strike-slip intraslab event located beneath Kodiak Island, Alaska down-dip of the locked portion of the Alaska-Aleutian megathrust (Hansen and Ratchkovski, 2001).

Thirdly, to our knowledge, these earthquakes are the first documented sizable earthquake doublet to involve a megathrust earthquake rupture, followed by an intraplate strike-slip earthquake tearing the subducting incoming slab. Earthquake doublets are pairs of events with comparable size and likely occur due to earthquake triggering interactions. Subduction earthquake doublets have been studied in the 2006-2007 Kuril and 2009 Samoa doublets (Lay, 2015). In the 2006-2007 Kuril earthquake doublet, a M_w8.4 megathrust earthquake was followed by a M_w8.1 earthquake rupturing an outer trench-slope normal fault, while in the 2009 Samoa earthquakes, a normal-faulting earthquake (M_w8.1) in the outer-rise region triggered a similarly sized thrust-faulting earthquake (M_w8.0) on the plate interface (Beavan et al., 2010). Therefore, detailed documentation of this doublet might contribute to the general understanding of the triggering mechanisms during doublets.

In this paper, we use geodetic observations to determine kinematic coseismic fault slip models of the M7.8, M7.6 earthquakes and the postseismic afterslip between two events. We investigate the major controls for the 2020 Shumagin earthquake doublet. We analyze the static fault slip distribution of both events using static GNSS offsets and InSAR surface displacement measurements. The earthquakes ruptured an area off the Alaska Peninsula covered with scattered islands, and incoherence due to water channels makes it challenging to estimate phase ambiguities during the InSAR phase unwrapping process. Hence, we take advantage of an improved Bayesian inversion of wrapped interferometric phase change observations (Jiang and González, 2020) to estimate the fault geometry and slip distribution. Our coseismic geodetic inversion results reveal that the Alaska megathrust has a complex down-dip segmentation. We propose a slab bend structure, which represents a major factor controlling the occurrence and interaction during this doublet, and contributes to the understanding of the mechanics of the subducting oceanic lithosphere in the central Alaska subduction zone.

2. Datasets

2.1. GNSS dataset

We used three-component coseismic offsets and postseismic time series from GNSS stations computed by the Nevada Geodesy Laboratory (Blewitt et al., 2018). The estimated coseismic offsets of the M7.8 and the M7.6 events were derived from 5-minute sample rate time series of GNSS stations, using 48 hours of data before and after the mainshock. The coseismic displacements were estimated by subtracting the median position after the mainshock from the median position before. For the postseismic displacements between the M7.8 and M7.6 events, the displacements can be observed in the GNSS time series of daily solutions. Taking station AC12 as an example, the M7.8 postseismic horizontal displacements in the 1, 2, 24 and 48 days are 0%, 4%, 19%, and 25% of the coseismic horizontal displacements of the M7.8 event. We model the 89-day postseismic deformation signal between July 22 to October 19 with an exponential transient decay function (Hearn, 2003), and the detailed steps are listed in Supplementary Section 1.

2.2. InSAR dataset

We imaged the ground surface displacement caused by the 2020 Shumagin earthquake doublet using InSAR. Satellite radar interferograms capture line-of-sight motion away or towards the satellite. We used 12 European Space Agency Sentinel-1 satellite interferometric wide swath mode images to make six interferograms from three different satellite tracks from July 10 to November 7, 2020 (Table S1). We used data from two parallel descending tracks to cover the epicentral area around the Shumagin and neighboring islands (track 73 and track 102). The ascending track 153 fully images the epicentral area. We processed the coseismic interferograms using the TopsApp module of the ISCE software (Rosen et al., 2012). We removed the topographic phase contribution in the interferograms using SRTM 30-m resolution DEM.

Our interferograms spanning the M7.8 event are dominated by the coseismic deformation signals (Fig. 1(c)-(f)). We generate a preseismic interferogram (Fig. S1) and the interferometric phase is dominated by the turbulent atmosphere delays. The two descending-track coseismic interferograms span less than 2 days of early postseismic deformation. However, for the coseismic interferogram in ascending track 153, the first available secondary image was acquired 48 days after the earthquake, hence it could be affected by postseismic deformation. We use the same strategy as described in Supplementary Section 1 to model the 48-day postseismic deformation signal (Fig. S9), and then we forward-simulate and remove the line-of-sight phase change from the ascending interferogram (track 152, Jul 22-Sep 08) during the first 48 days of the postseismic period. Although the correction is relatively small, our approach reduces the leakage of postseismic deformation into our coseismic models.

For the interferograms covering the M7.6 event, the interferometric phase observations are also dominated by the coseismic deformation signals. The estimated postseismic relaxation time for the M7.8 event is approximately 40 days, while the acquisition dates of the primary images of the interferograms for the M7.6 event are 84 and 86 days after the M7.8 event, that is 5 and 3 days before the M7.6. Therefore, any M7.8 postseismic deformation signal can be considered negligible. The interferograms spanning the M7.6 event might contain 7, 9 and 19 days of postseismic deformation of this event. However, we did not find clear transient displacement signals either in the postseismic interferograms or GNSS time series during the M7.6 early-postseismic period, so we performed no corrections on the coseismic interferograms.

3. Methodology

3.1. Fault geometry: Non-linear surface displacement inversion

To determine the fault geometry of the ruptures, we invert for an elastic uniform slip rectangular dislocation model. The sparse spatial distribution of the GNSS stations does not allow us to tightly constrain the fault geometry (Fig. S2). Thus, we take advantage of independent high-spatial-resolution InSAR observations over the Shumagin Islands and the imaged far-field surface deformation over the Alaska Peninsula to refine the rupture fault geometry.

Standard modeling approaches of InSAR observations require unwrapping the wrapped phase from [-π,π] to the absolute unwrapped line-of-sight displacements. However, phase unwrapping is an ill-posed problem requiring integration along a path connecting pixels. In the Shumagin islands, the incoherence due to water channels between islands makes the phase unwrapping especially challenging. Any phase unwrapping of coseismic interferograms might contain unknown multiples of 2π between islands (Fig. S12) due to the dense gradient of fringes. Instead, our method skips the phase unwrapping step, and directly inverts for fault source parameters by applying the WGBIS method, a Bayesian algorithm that minimizes the weighted wrapped phase residuals (Jiang and González, 2020). Now, using the wrapped InSAR phase and GNSS offsets, we can constrain more tightly the fault geometry parameters (Fig. 2).

3.2. Distributed slip models

Next, we propose an extension to the WGBIS method and estimate distributed fault slip on the WGBIS-estimated fault geometry, directly from

InSAR wrapped phase observations applying a novel physics-based fault slip regularization. The traditional kinematic fault slip inversion method uses static observations to solve for the slip displacements but neglected to consider the driving forces or stresses that cause these motions. To characterize the earthquake source, Brune (1970) introduced a source model where the source stress drop and fault dimensions are related in the source spectrum. The Brune model for the far-field displacement assumed a sudden stress drop across the entire crack during a shear dislocation in a circular crack. Recently, a more physical analytical crack model is proposed to describe the relationship between stress and slip on the fault in a laboratory experiment (Ke et al., 2020). Instead of a uniform stress drop across the whole fault plane, the model of Ke et al. (2020) allows a nearly constant stress drop in the crack center while keeping the stress concentration at the rupture tip finite, and it retains a smooth transition in between. The preferred shape of the crack model, an ellipse, is supported by mechanical considerations (Sendeckyj, 1970). Thus, we expand the one-dimensional slip profile in Ke et al. (2020) to a two-dimensional model with an elliptical shape, by assuming one of the focal points of the ellipse to be the crack centre and the elliptical perimeter to be the crack tip. Therefore, the slip distribution s on the fault plane is controlled by a very reduced set of parameters, and our crack model contains only seven parameters.

$$s = \mathbf{f}(x_0, y_0, a, e, \lambda, d_{max}, \theta) \tag{1}$$

where x_0, y_0 are the locations of the focal point; a and e are the semi-major axis and eccentricity of the ellipse; λ is the ratio controlling the displacement transition from the center to the edge of the elliptical crack; d_{max} is the maximum slip; θ is the rake angle. The detailed steps of forward simulation are listed in Supplementary Section 2. We also design synthetic tests to validate our approach, and compare the performance with respect other slip-inversion methods (Fig. S14).

We rationalize our choice for a simple elliptical crack model, firstly because the resolution power of InSAR and GNSS data to constrain the subsurface slip distribution decrease with the fault depth and off-shore distance. Deeper earthquake sources will produce less surface deformation than shallower events of the same size, and hence the detailed distributions of fault slip of deep sources are not well resolved (Funning and Garcia, 2019). Second, the published M7.8 earthquake coseismic slip distributions agree on the most notable feature: a high fault slip area with rather smooth slip distribution on the plate interface beneath the Shumagin Islands (Crowell and Melgar, 2020, Ye et al., 2021). This first-order pattern is well resolved by our distributed fault slip model. Third, a simple circular crack is also a widely accepted model to estimate the stress drop of earthquakes using the observed seismic spectra (Brune, 1970). In addition to the desirable physics-based properties (finite shear stress at the crack tip), another advantage of this method is its low dimensionality. The model is parametrized using fewer parameters than usually needed to describe the spatial pattern of slip distributions. Previous inversion algorithms using deterministic or Bayesian approaches allow for highly complex patterns of slip distributions by allowing unconstrained or regularized slip distributions (Fukahata and Wright, 2008). However, those methods are solving very high dimensional problems with larger associated null-spaces, and are also computationally more intensive.

3.3. Coulomb stress models

The Coulomb stress theory has been extensively applied to study the interaction between earthquakes. Coulomb stress change induced by fault slip is a quantitative measure that has been correlated with the aftershock distribution, seismicity rate changes and earthquake triggering. Usually, more aftershocks occur in the high stress-change region (Dieterich, 1978). It is thought that increases in Coulomb stress of 0.01 MPa are sufficient to trigger events (King et al., 1994). In our study, we calculate the Coulomb stress changes due to the M7.8 event and investigate whether the M7.8 earthquake and its afterslip promoted failure of the subsequent M7.6 event. We use the Coulomb 3.3 program to carry out the stress calculations, which is based on the dislocation model algorithms (`https://www.usgs.gov/software/coulomb-3`).

4. Results

4.1. Coseismic model for the M7.8 earthquake

The Shumagin earthquake nucleated near the eastern edge of the Shumagin seismic gap (Ye et al., 2021). Our static surface displacement inversions suggest that the coseismic rupture extended for 112±2 km to the WSW from the location of the USGS hypocenter (red rectangles in Fig. 2), with an average pure thrust slip of 1.5±0.1 m, corresponding to an estimated M7.8. The buried rupture extended down-dip to 44±2 km and up-dip up to 14±2 km depth and did not break the seafloor at the Alaska-Aleutian trench. A remarkable feature of our inversion results is that the inferred fault geometry requires a relatively steep dip angle (26°±0.5°, Fig. 2(b)), steeper than the widely used Slab2 subduction model ($\sim$15°, Hayes et al. (2018)). We further investigate this feature by separately inverting for the fault geometry using GNSS coseismic offsets only, InSAR wrapped phase only and both observations. In all cases, the obtained fault geometries are consistent with a 25°-to-28° fault rupture plane. The GNSS only inversion suggests a slightly steeper fault dip angle (Fig. S2) than the 26°±0.5° dip angle, obtained using only the InSAR wrapped phase or both datasets (Fig. S3-S4).

Next, we use our estimated fault geometry model to refine the location and pattern of coseismic slip during the earthquake. We tested two different 3D fault geometry parameterizations. The first 3D fault geometry, based on the estimated fault geometry, contains two segments, as shown in Fig. S13. A deeper segment dipping 26° from 14 to 44 km depth using the optimal rectangular dislocation plane estimated by the non-linear inversion, and then a shallower segment connecting the top edge of the rectangular plane to the trench. These fault planes were then discretized into a triangular mesh with patch dimensions of $\sim$20 km. A second geometry was obtained based on the Slab2 model for the Alaska megathrust, which has an average dip of 15° from 20 to 50 km at depth (Hayes et al., 2018).

We solve for the slip distribution of the elliptical rupture model on our proposed fault geometry. Fig. 3 shows the observed and modeled GNSS displacements and the wrapped interferometric phase, as well as the residuals using the proposed down-dip structure. The modeled phase is consistent with the observed phase. The root-mean-square (RMS) of the GNSS residuals in the east, north and vertical directions are 0.3, 0.3 and 0.6 cm, and corresponding to data variance reductions of 98%, 99%, and 97%. The GNSS offsets can be fit comparably well with our proposed geometry and Slab2 geometry (Fig. S5-S7). However, the distributed slip model on the Slab2 geometry cannot reproduce the InSAR surface displacement patterns as well as those with the optimized, steeper fault geometry (Fig. S5-S6), and the variance of InSAR wrapped phase residuals is 1.02 rad (or 0.91 cm) for the inversion on the Slab2 geometry, while 0.87 rad (or 0.77 cm) for the inversion on our proposed fault geometry. Moreover, the posterior probability distribution functions on the elliptical rupture model parameters are less well resolved for the Slab2 fault parameterization (Fig. S7). Our final slip model (Fig. 5) shows a patch of large slip near the hypocenter and below the Shumagin Islands, consistent with kinematic coseismic slip models constrained using near-field high-rate GNSS and strong-motion data showing a more broadly distributed slip (Crowell and Melgar, 2020). The rupture area with significant slip (>1.5m) is largely overlapped with the finite-fault slip model (>1.5m) using joint inversion of teleseismic P and SH waves and static displacements from regional GNSS stations (Ye et al., 2021). However, the finite slip model in Ye et al. (2021) imaged two separated ruptures with large slip, one below the Shumagin Islands and the other closed to the epicenter, while our rupture model preferred a wider and compact slip distribution. Another discrepancy between two rupture models is several smaller patches revealed by Ye et al. (2021), including one patch located to the west, one patch near the border of Shumagin and Semidi segments, and two patches in the downdip direction. The fault slip distribution inverted from GNSS and three interferograms is shown in Fig. 5, with peak slip 1.8 m, and the average slip 0.7 m. The total geodetic moment is 6.12×10^{20} Nm, which is equivalent to M_w7.79, a value consistent with the seismic moment magnitude of M_w7.8. The estimated rupture centroid is located at [158.834°W, 55.130°N] and the centroid focal depth is 32 km, which is deeper than the 28 km estimated by USGS and 19 km away from the USGS-estimated hypocenter, [158.596°W, 55.072°N], in the northwest direction.

4.2. Postseismic model for the M7.8 earthquake

The M7.8 postseismic phase is important to study the whole doublet sequence, so we quantify the amount and distribution of early postseismic slip caused by the M7.8 event. As afterslip is unlikely to be compact, and may fully surround the coseismic rupture, the spatial distribution of postseismic slip is resolved by using the slip inversion package, SDM (Wang et al., 2013). This method incorporates a stress smoothing factor to regularize the slip distribution. A smoothing factor 0.3 is applied which is determined from the trade-off curve between data misfit and model roughness (Fig. S10(a)). We assume that afterslip dominates the observed surface deformation during the 89-day-long period between the M7.8 and the M7.6 events. Afterslip describes postseismic fault motions occurring near the mainshock rupture regions over several months to several years. Postseismic offsets are estimated by fitting the daily GNSS data from July 22 to October 19 with a simple exponential model and then inverted for the postseismic slip distribution. Compared with the coseismic model 3D fault discretization, the subduction zone interface is extended along strike and down-dip to investigate the distributed postseismic slip over a wider area of the plate interface. The model predictions agree well with GNSS observations (Fig. S8), and the RMS of the GNSS residuals in the east, north and vertical directions are 0.6, 0.6 and

0.7 cm, respectively.

We find the postseismic afterslip region occurs in three primary regions: updip, east and west of the coseismic rupture (Fig. 5). One significant feature is the afterslip at shallow depth (6-14 km), just top of the most significant coseismic slip, while no clear afterslip occurred below the coseismic rupture zone. Two patches with dimensions of $\sim$60 km and 0.20 m slip are inferred to have slipped aseismically east and west of the coseismic rupture zone at 30-70 km and 14-44 km depth. The 3-month postseismic slip has a cumulative geodetic moment of 3.1×10^{20} Nm, corresponding to $M_w7.60$, assuming a variable crustal shear modulus with depth from CRUST 1.0. We also find overlaps between coseismic and postseismic slip regions, and the overlap area is located at the eastern and western end of the elliptical rupture in our coseismic slip model, and at two separated ruptures in Ye et al. (2021) coseismic slip model. This might suggest areas with less coseismic slip continues to be active during the postseismic period.

Crowell and Melgar (2020) estimated the first 10 days of the postseismic afterslip, finding that the majority of afterslip is concentrated downdip of the mainshock between 40-60 km depth. The afterslip region east of the mainshock in their model is generally consistent with our afterslip model. Recently, Bin Zhao et al. (*pers. comm., 2021*) applied additional constraints to regularize the afterslip distribution, where they considered both stress-driven frictional models and kinematic inversions in which no slip is allowed within the coseismic peak slip zone. Their models suggest possible afterslip in the up-dip area of the M7.8 earthquake, which is consistent with our finding.

4.3. Coseismic model for the M7.6 earthquake

To parameterize the geometry of the October 19 2020 M7.6 Shumagin earthquake, we consider the spatial distribution of its aftershocks. Most of these aftershocks occurred at the western edge of the coseismic slip area of the M7.8 event. Aftershocks are aligned in a north-south direction, parallel to the plate convergence direction. We first approximate the dimensions of the rupture area using the aftershock locations in the first two days after the M7.6 event. The estimated rupture area dimensions from the aftershocks are 100-150 km long and 50-60 km wide and dipping 38° to the east. Those parameters are consistent with the focal mechanism from GCMT catalog (dip=49°, strike=350°) and the inverted parameters for a rectangular dislocation source (length=66 km, width=28 km, top depth=19 km, bottom depth=39 km, dip=45°, strike=358°, strike slip=2 m). Our slip model reproduces well the coseismic deformation observed by GNSS and InSAR (Fig. 4 and Fig. S11).

The coseismic slip model shows right-lateral strike-slip motion on a fault plane perpendicular to the Alaska subduction zone, consistent with the distribution of the aftershocks. The aftershocks following the M7.6 event occurred at the periphery of the coseismic rupture (Fig. 1(a)), effectively extending the latter farther to the south and were dominated by strike-slip rupture mechanisms with east-dipping north-south-striking nodal planes. The total moment release from the coseismic slip was 2.7×10^{20} Nm, assuming a variable crustal shear modulus with depth based on the CRUST 1.0 model. The corresponding moment magnitude is M_w=7.55, in reasonable agreement with the seismically determined value.

Our model suggests that the rupture zone is located from 19 to 39 km at depth, beneath the slab interface (Fig. 2(c)). This reveals that the M7.6 strike-slip earthquake ruptured the subducting oceanic slab, rather than the forearc. This is also confirmed from the focal depth range of the aftershocks. 70% of the M2.5+ aftershocks in the first 2 days after the M7.6 event occurred at 20-40 km depth. A significant non-double-couple component in the moment tensor, the substantial tsunami and the residuals of the GNSS vertical component (Fig. 4(a)) indicate that another shallow rupture segment parallels to the trench might exist (Lay, 2021), but our geodetic inversion cannot resolve a second segment at shallow depth. Our inversions for two segments using the geodetic data are not stable, which might be limited by the minor deformation signals on the islands.

5. Discussion

5.1. Influence of slab geometry on the rupture characteristics of the M7.8 earthquake

Our preferred coseismic rupture model constrains the deep structure of the Alaska megathrust along the Shumagin segment. It reveals a $26°\pm0.5°$ dipping interface from 14 to 44 km depth. The megathrust interface at shallower depths is a gentler dipping segment ($\sim 8°\pm4°$) of 90 km width, connecting the up-dip edge of the rupture to the trench (Fig. 2). This plate-interface geometry substantially deviates from the most recent subduction interface model Slab2, which is based on regionally and globally located seismic events (Hayes et al., 2018). The Slab2 model suggests a 15° dip in the depth range from 20 to 50 km. This low dip angle can result from few seismicity in this region, and smoothness constraints are applied to the subduction zone model, which might not resolve length-scales similar or smaller than those of the Shumagin gap (100-200 km). From moment tensor solutions, the dip angles are in the range of 17°-20° (Ye et al., 2021), which is also lower than the dip angle retrieved from geodetic observations. It is widely reported that a discrepancy in dip between the moment tensor solution and that of geodetic inversions (Weston et al., 2014). One potential reason leading to the dip angle uncertainty in moment tensor is its dependence on the moment (Tsai et al., 2011) or assumed initial depth (Duputel et al., 2012), but this uncertainty is commonly not quantified and reported in published works.

Another potential cause of dip angle discrepancy is the underestimated dip angle uncertainty in our model due to simplified assumptions. The true uncertainties of fault source parameters depend on various assumptions (e.g., fault geometry, elastic Earth structures), and the simplified assumptions might lead to the underestimation of model uncertainties. (1) Uniform fault slip on a rectangular plane is assumed when retrieving the dip angle in this research, while the dip angle might be biased for a spatially variable slip distribution. A synthetic experiment shows that, for the M7.8 earthquake, the inversion with rectangular uniform slip might lead to an overestimated dip angle $\sim$2.5° (Fig. S15 and Supplementary Section 3). A more reliable uncertainty in dip angle can be gained by inverting the fault slip distribution and dip angle simultaneously (Fukuda and Johnson, 2008). (2) A homogeneous half-space model is applied when estimating the fault model in this research, while a realistic earth structure is more complex. In Supplementary Section 4, an experiment is designed to investigate the effect of different earth models on the surface displacements. The results reveal that, for 3 GNSS stations on Shumagin islands (AC12, AC28, AB07), the relative differences of surface displacements are 15%$\sim$50%, 10%$\sim$30% and 2%$\sim$5% in east, north and vertical directions using homogeneous half-space and multi-layered models (Table S5). The synthetic experiments above suggest an underestimated uncertainty of fault dip angle with assumed simplified models, and this underestimated uncertainty can be improved by considering more realistic fault models and medium properties.

Seismic reflection imaging along profiles across the Shumagin segment suggests a geometry similar to our inversion results (Li et al., 2015). In Fig. 2(b), we show the interpreted seismic reflection data from Line 4 of Li et al. (2015). Line 4 is in close proximity to the M7.8 rupture area, at the boundary of the Semidi segment and Shumagin seismic gap. The seismic reflectors are consistent with our inferred fault geometry. Our plate interface geometry also agrees with a fault geometry grid search using GNSS vertical coseismic offsets caused by the M7.8 earthquake by Crowell and Melgar (2020). Their dislocation models also support a 25° dip fault geometry, with an up-dip edge at 21$\pm$2 km and extending down to 45$\pm$5 km depth.

We also note that the bottom end of the M7.8 rupture (44 km) likely reached the down-dip limit of the locked seismogenic zone, and this pattern has been noted in other subduction zones (Simoes et al., 2004). Recently, Shillington (2021) analyzed the seismic reflection data near Line 5 (Fig. 2(a)) and found the continental Moho depth at 35 km, with less uncertainties than Line 4 (Li et al., 2015). If this is confirmed, it might suggest that part of the coseismic slip extended downdip of the continental Moho (or mantle wedge corner). This coseismic slip feature was previously observed in very large megathrust events, e.g., the 2010 M8.8 Maule, Chile, earthquake (Weiss et al., 2019). One of the explanations could be that hydrated materials (e.g., serpentinites) along the base of the mantle wedge control the frictional properties of the megathrust, and allow the propagation of large ruptures, even though the megathrust downdip of the mantle wedge corner is predominantly velocity strengthening (Kohli et al., 2011).

Our findings suggest that the fault geometry controls the rupture size and extent. A similarly large buried rupture was observed during the 2015 Gorkha, Nepal earthquake on a continent-continent subduction zone (Elliott et al., 2016). Hubbard et al. (2016) developed a fault morphological model consisting of two ramps and found that the location and shape of coseismic fault slip (>1m) match well with the location and shape of the middle decollement bounded on both sides by ramps. Therefore, they proposed that the variations in fault dip angle controlled the shape and size of the mainshock rupture in this continental megathrust earthquake. Decollement-ramp structures formed in subducting sediments are not rare in global subducting zones (Seno, 2017). About 1 km-thick subducting sediments were inferred from seismic reflection data beneath the eastern Shumagin gap (Li et al., 2018) and clear variations of the megathrust dipping angle were revealed at 7 km and 17 km (Li et al., 2015), which is consistent with the top rupture depth at 14 km. Although the uncertainty of top depth can be underestimated due to the assumed simplified model, a synthetic experiment suggested the underestimation of top depth is $\sim$2 km (Fig. S15 and Supplementary

Section 3), so a significant slip change still occurred at depth where dip angle changes abruptly (Fig. S16). In summary, the variation in fault orientation with depth was likely a controlling factor limiting the extent of the Shumagin rupture.

5.2. The M7.6 slab-tear earthquake source region

If we assume that the M7.6 earthquake occurred on a pre-existing fault plane, prior to being subducted, this fault had a strike of 15° and a dip of 60°. This strike angle is consistent with the spreading of the Kula-Resurrection ridges, which were subducted beneath the Aleutian Islands in the present days (Fig. 7(a)). Fuston and Wu (2020) reconstructed the plate tectonics history of western North America and proposed that these ridges were active from 60 to 40 Ma, producing north-south striking faults through the seafloor spreading, and have been inactive since ∼40 Ma. The inferred dipping angle of the pre-existing fault is consistent with the dip angle of mid-ocean-ridge normal faults. The pre-existing faults are unlikely to be formed in the outer-rise region because the outer-rise bending faults are parallel to the trench with approximately east-west strike directions (Shillington et al., 2015). The pre-existing faults are unlikely to have formed along the Pacific-Kula ridge or the Pacific-Farallon ridge, because the orientation of the magnetic anomalies (east-west and northwest-southeast) are inconsistent with the eventual strike of the M7.6 ruptured fault. In addition, previous studies reported the possibility of subduction earthquakes on the reactivated fracture zones. For example, the 23 January 2018 M_w 7.9 Gulf of Alaska earthquake is interpreted as the reactivation of a strike-slip fault in the outer-rise region (Krabbenhoeft et al., 2018). The June 4 2000 M_w7.9 Sumatra earthquake is another example but on the landward side of the subduction trench (Abercrombie et al., 2003). The reactivation of the incoming (oceanic) fabric is also suggested by the microseismicity occurrence, which is favored in the parallel orientation of the convergence vector (Lange et al., 2010).

In addition, our M7.6 fault model is correlated with the location of a low seismic-velocity anomaly, which has been attributed to higher slab hydration (Li et al., 2020). Li et al. (2020) imaged the crust and uppermost mantle structure of the Alaska subduction zone using ocean bottom seismographs and broadband seismic stations. They constructed a 3-D shear velocity model, where one trench-normal profile (TT1) is just <5 km away from the M7.6 rupture area. They found upper mantle shear-velocity reductions along this profile of about 15% (from $\sim$4.6 to $\sim$3.9 km/s), which extends more than 12 km beneath the Moho. In other regions along the Alaska subduction zone (e.g., the Semidi segment), the upper mantle velocity reduction is only about 11% (from $\sim$4.6 to $\sim$4.2 km/s). They interpret this feature as evidence of stronger hydration of the incoming plate along the Shumagin seismic gap. Furthermore, in the outer-rise region of the Shumagin Islands (Line 5 in Fig. 2(a) and Fig. 4(a)), Shillington et al. (2015) found a P-wave velocity reduction in the upper mantle from 8.25 to 7.75 km/s, associated with abundant bending faults. These observations lend further support to the existence of faults in the subducted slab beneath the Shumagin Islands, which might have played a major role in the location of seismogenic ruptures.

Spatial variations of elastic coupling along the megathrust interface could cause shear stress on the location of the M7.6 event. Herman and Furlong (2021) present models that simulate the effect of laterally variable coupling.

The preferred models represent the Semidi segment to be highly coupled while the Shumagin segment has low coupling. The lateral displacement variations can impose large-magnitude, right-lateral shear stresses on the M7.6 rupture plane geometry, assuming the target fault plane was north-south striking and east dipping with a dip angle 50°. However, we note that the available geodetic observations infer only 30%±10% coupling in the western portion of Semidi segment (Drooff and Freymueller, 2021) which is much lower than the 100% assumed by Herman and Furlong (2021), for the whole Semidi segment. Therefore, interseismic coupling variation between the Semidi and Shumagin segments may contribute to the shear stress accumulation on the M7.6 rupture plane, but geodetic evidence suggests this contribution may be more modest in magnitude. Hence, lateral variations of coupling and the existence of structural weaknesses could explain the occurrence of the M7.6 slab breaking event, which broke the entire seismogenic thickness.

5.3. Mechanisms for the interaction between the two earthquakes

Earthquake doublets are not uncommon and suggest short-term fault interactions and triggering. Lay (2015) compiled 7 pairs of earthquake doublets in subduction zones, where he proposed that stress transfer and triggering interactions are clearly demonstrated by several doublet sequences and the complexity of faulting of many of the events. To investigate the possible relationship between these events, we calculate the stress perturbations on the M7.6 event associated with the Jul 22 2020 M7.8 coseismic and postseismic slip (Fig. 6(d)). We utilize the inferred slip distribution from our inversion model for the M7.8 event. Then, we compute the stress change on the estimated fault plane of the M7.6 event. We extend the M7.6 rupture fault plane along dip from the surface down to 60 km depth, and compute the stress change on a regular grid with 5 km-wide patches. The M7.8 earthquake caused a shear stress increase of 0.1 MPa and tensile normal stress increase of 0.3 MPa around the hypocenter, while the contributions from the postseismic slip are almost neutral. Our Coulomb stress models suggest that the second, M7.6 intraslab, earthquake was likely triggered by the elastic stress changes transferred by the slip during the M7.8 coseismic slip on the megathrust interface, with postseismic deformation processes possibly explaining the ~3-month delay in the occurrence of the large intraslab event. At the time of the writing, a M8.2 earthquake occurred at the Semidi segment on Jul 29, 2021 (Fig. 5(a), `https://earthquake.usgs.gov/earthquakes/eventpage/ak0219neiszm/executive`). We utilize the same method to calculate the stress perturbations on the M8.2 event. The M7.8 earthquake caused a shear stress increase of 0.03 MPa and tensile normal stress increase of -0.01 MPa around the hypocenter, while the contributions from the postseismic slip are 0.01 MPa increase in shear and normal stress. This indicates that both M7.8 coseismic and postseismic slip on the megathrust interface could have triggered the M8.2 event.

6. Conclusions

We conclude that the 2020 Shumagin earthquake doublet represents a rare example of two deeply buried ruptures on a subduction megathrust and an oceanic intraplate strike-slip fault (Fig. 7(b)). The first M7.8 earthquake partially ruptured the Shumagin seismic gap, along a 112 km-long, 65 km-wide section, extending from 14 to 44 km depth. The second M7.6 event was likely triggered by static stress changes due to the M7.8 coseismic slip. The M7.6 broke the incoming oceanic plate at moderate depths from 19 to 39 km along a north-south striking and east-dipping, right-lateral strike-slip fault. We propose that the Shumagin gap is segmented and has variable mechanical characteristics. The M7.8 earthquake ruptured a distinct eastern segment of the Shumagin gap, while the western segment and shallow portions remain unruptured. We highlight that the inferred rupture geometry of the M7.8 event is substantially steeper compared to the Slab2 model. The variations of down-dip megathrust structure of the Shumagin segment might have implications for seismo-tectonics and tsunami hazard of this segment of the Alaska-Aleutian subduction zone, e.g., by controlling the degree of coupling and seismic segmentation of the megathrust interface (Fournier and Freymueller, 2007), and influencing coseismic and postseismic slip distributions (Crowell and Melgar, 2020). In addition, we identify Kula-Resurrection ridge fault structures imprinted in the oceanic lithosphere as the likely earthquake source plane reactivated during the M7.6 event. Our study highlights that the reactivation of such oceanic lithospheric structures might pose an important seismic hazard in subduction zones, and might represent favorable pathways for fluid flow and dehydration of the subducting slab.

7. Acknowledgments

This research was supported by the Natural Environmental Research Council (NERC) through the Centre for the Observation and Modelling of Earthquakes, Volcanoes and Tectonics (GA/13/M/031) and the LiCS large grant (NE/K011006/1). This research was also supported by a Chinese Scholarship Council-University of Liverpool joint scholarship awarded to YJ (201706450071). PJG contribution was supported by the Spanish Ministerio de Ciencia e Innovación research project, grant agreement number PID2019-104571RA-I00 (COMPACT) and the Beca Leonardo a Investigadores y Creadores Culturales 2020 of the Fundación BBVA. RB acknowledges support by NSF award EAR-1801720. Global Centroid Moment Tensor (GCMT) Solutions are from https://www.globalcmt.org/CMTsearch.html. Earthquake information is based on the catalogs from U.S. Geological Survey (USGS) (https://earthquake.usgs.gov/earthquakes). Copernicus SAR data are retrieved from `scihub.copernicus.eu`, and 6 interferograms can be downloaded from Zenodo (`https://doi.org/10.5281/zenodo.5722342`). The GNSS stations with three-component coseismic offset estimates for Jul 22 2020 M7.8 event and Oct 19 2020 M7.6 event are retrieved from `http://geodesy.unr.edu/news_items/20200723/us7000asvb_5min_rapid_20200723.txt` and `ftp://data-out.unavco.org/pub/products/event/cwu_201019_2055_eq59_coseis_final.evt`. The 21 GNSS stations with three-component daily offsets to estimate the postseismic decay time are retrieved from Nevada Geodetic Laboratory (`http://geodesy.unr.edu/`). The Subduction zone geometry model is retrieved from Slab2 (`https://www.sciencebase.gov/catalog/item/5aa1b00ee4b0b1c392e86467/`). The bathymetry data is retrieved from SRTM30_PLUS (`https://topex.ucsd.edu/WWW_html/srtm30_plus.html`). The earthquake catalog is retrieved from USGS (`https://earthquake.usgs.gov/earthquakes/search/`). The coastal data is retrieved from NOAA (`https://www.ngdc.noaa.gov/mgg/shorelines/`). This is a contribution of the CSIC Thematic Platform PTI-Teledect (`https://pti-teledetect.

csic.es/). CRUST 1.0 model is retrieved from https://igppweb.ucsd.edu/~gabi/crust1.html. The authors thank the Editor Jean-Philippe Avouac, Jeffrey Freymueller, Tim Wright, and an anonymous reviewer for their insightful comments. The authors thank Lingling Ye for providing the coseismic slip model for the 2020/07/22 M7.8 earthquake as shown in Fig. 5(b). The authors also thank Lucía Pérez-Díaz for her help on the plot of Fig. 7(b).

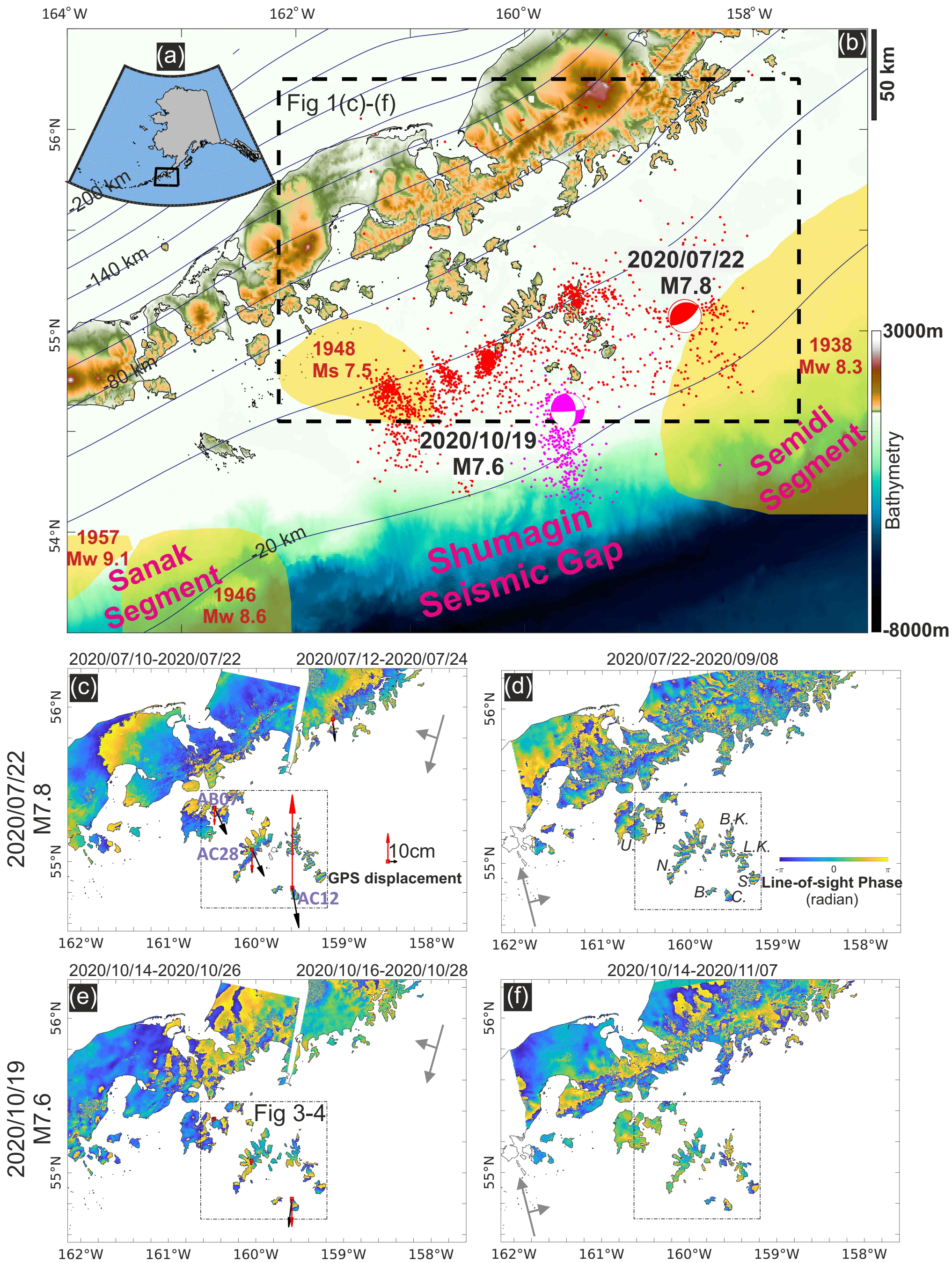

Figure 1: Tectonic background and geodetic observations of the Shumagin earthquake doublet, 2020/07/22 M7.8 earthquake and 2020/10/19 M7.6 earthquake.

Figure 1 (continued): (a) inset shows the Aleutian subduction zone. Image (b) shows historic ruptures as shaded yellow areas, on top of the bathymetry as the background. The Shumagin seismic gap is the 200 km-long region between the 1946 $M_w8.6$ and the 1938 $M_w8.2$ earthquakes. The M7.8 and the M7.6 events are plotted as red and magenta beachballs. The first 2-day and 3-month aftershocks following the M7.8 event are plotted as red and gray dots. The first 2-day aftershocks following the M7.6 event are plotted as magenta dots. The dashed box shows the boundary for images (c)-(f). Image (c) shows the wrapped phase of two descending interferograms, 2020/07/10-2020/07/22 (Track 73) and 2020/07/12-2020/07/24 (Track 102). The arrows show the GNSS displacements retrieved from Nevada Geodesy Laboratory, red for vertical, and black for horizontal displacements. AB07, AC28 and AC12 are three GNSS stations with the most significant movement. GNSS displacement at [158.5W,55N] is the unit displacement vector for 10cm vertical and horizontal displacement. The dotted-dashed box marks area in Fig. 3 and Fig. 4. Image (d) shows the ascending interferogram 2020/07/22-2020/09/08 from track 153. Images (e) and (f) are same with images (c) and (d), but three interferograms covering the M7.6 event, of two descending interferograms, 2020/10/14-2020/10/26 (Track 73) and 2020/10/16-2020/10/28 (Track 102), and one ascending interferogram, 2020/10/14-2020/11/07 (Track 153). Island abbreviations: U.: Unga; P.: Popof; N.: Nagai; B.K.: Big Koniuji; L.K.: Little Koniuji; B.: Bird; C.: Chernabura; S.: Simeonof.

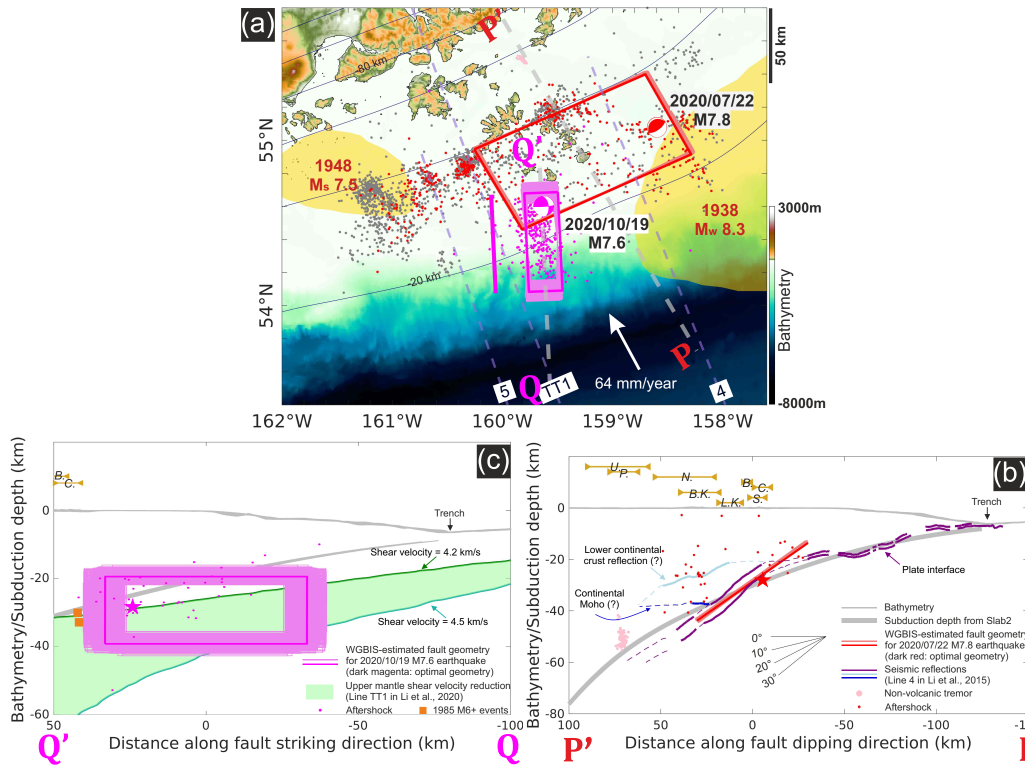

Figure 2: Preferred geodetic fault model constrained using InSAR wrapped phase and GNSS. In image (a), red and magenta rectangles outline the ensemble of inverse bayesian fault geometry models for the M7.8 and the M7.6 earthquakes. The black line west of the magenta rectangle indicates its projection to the surface. The dashed purple lines 4, 5 and line TT1 indicate the position of a seismic reflection line from Li et al. (2015) and a shear velocity profile from Li et al. (2020); the dashed gray lines are profiles PP' and QQ' shown in (b) and (c). Image (b) shows a cross-section of the inferred fault geometry models of the M7.8 earthquake projected to profile PP'. We also show the geophysical interpretation of the reflection lines (Line 4 and Fig. 5 in Li et al. (2015)), and locations of tremor (Brown et al., 2013). The cross-section also shows Slab2 model (depth to the top of subducting plate) and the bathymetry along profile PP'. Brown lines show the projected location of islands with the same abbreviations as Fig. 1(d). Image (c) shows a cross-section of the inferred fault geometry models of the M7.6 earthquake projected to profile QQ'. We also show the shear velocity reduction zone within upper mantle, constrained by the shear velocity 4.2 km/s and 4.5 km/s and digitized from Li et al. (2020).

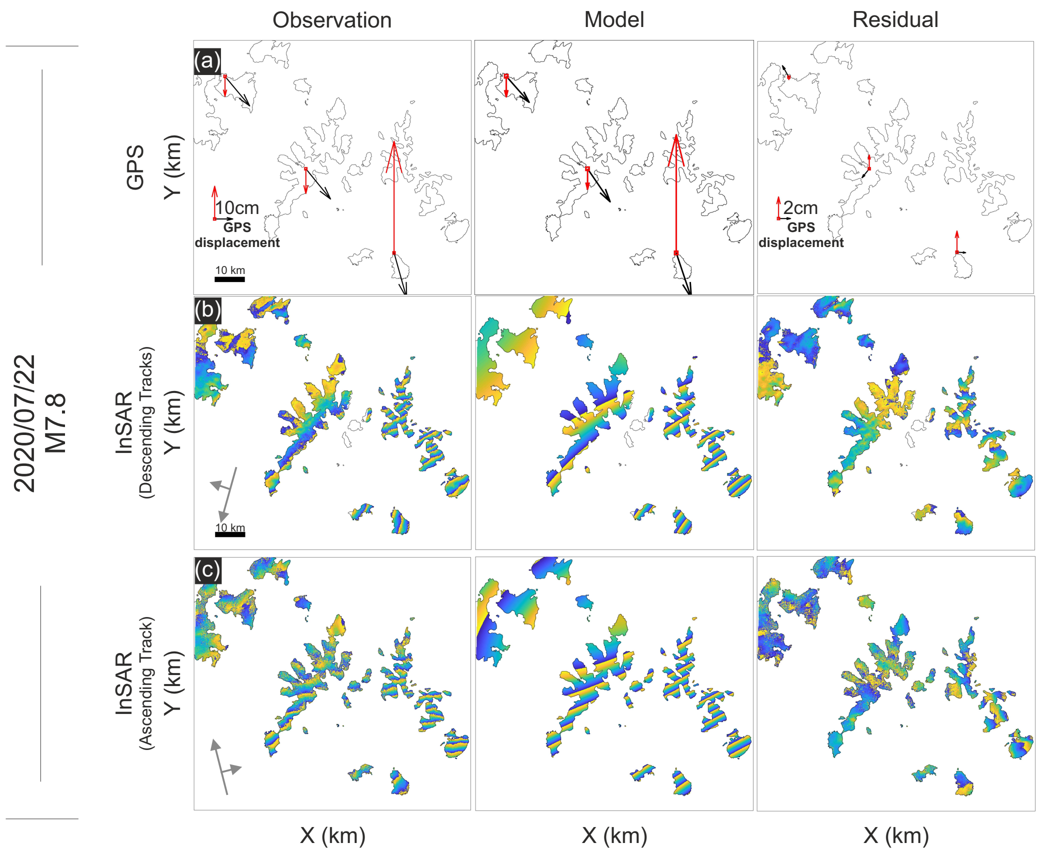

Figure 3: The observed and modelled GNSS displacements and wrapped interferometric phase for 2020/07/22 M7.8 earthquake. Images in the left column present the GNSS observations and the observed wrapped phase for the interferograms along 2 descending tracks, as shown in the dotted-dashed box in Fig. 1(c)-(f). Images in the middle column are the modelled GNSS and wrapped phase based on the optimal slip distributions. Images in the right column are the residual between observations and model.

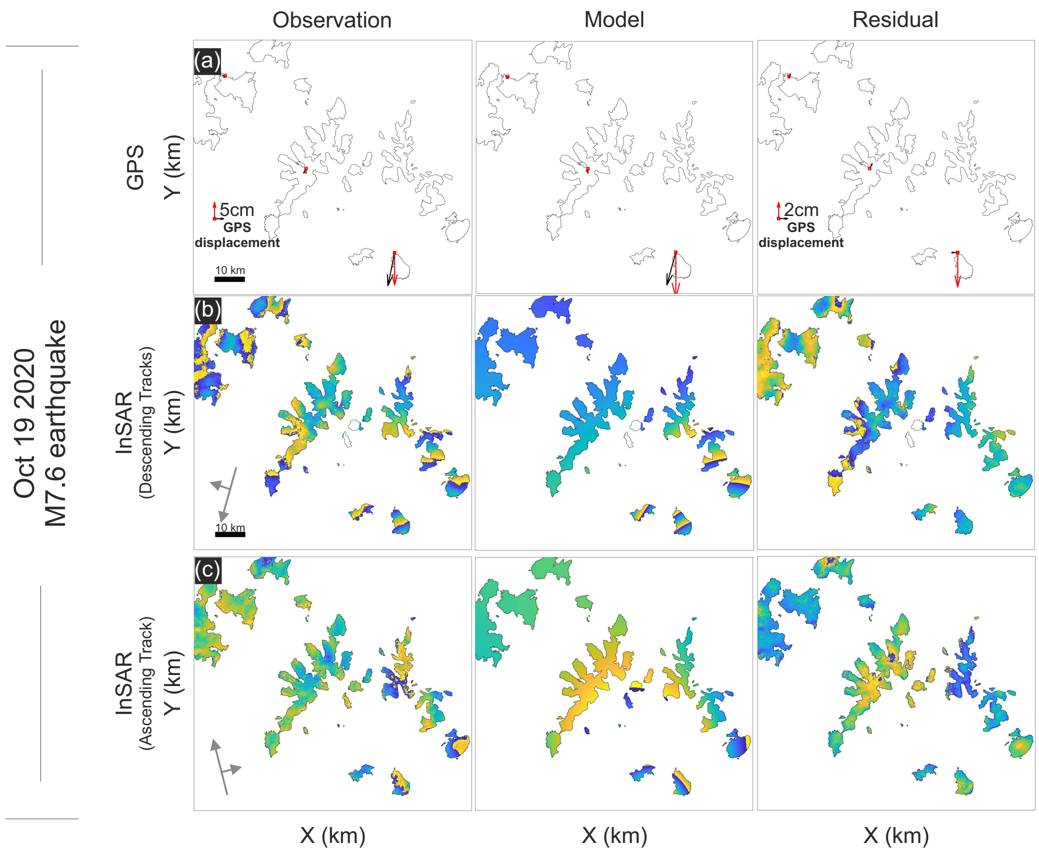

Figure 4: The observed and modelled GNSS displacements and wrapped interferometric phase for 2020/10/19 M7.6 earthquake. Images in the left column present the GNSS observations and the observed wrapped phase for the interferograms along 2 descending tracks, as shown in the dotted-dashed box in Fig. 1(c)-(f). Images in the middle column are the modelled GNSS and wrapped phase based on the optimal slip distributions. Images in the right column are the residual between observations and model.

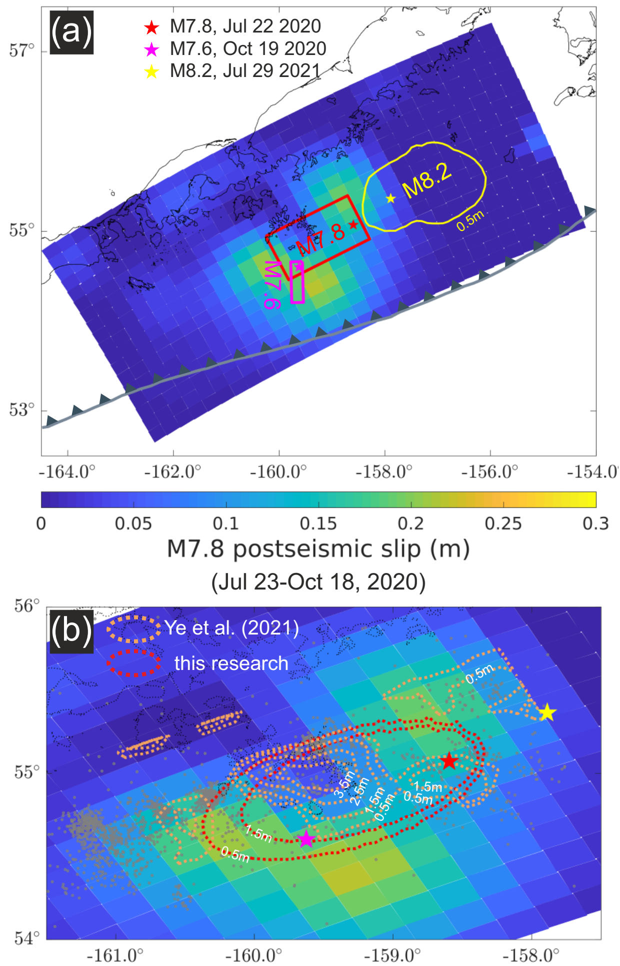

Figure 5: 2020 Shumagin earthquake doublet inferred fault slip distribution. In image (a), the epicenters of the 2020/07/22 M7.8 earthquake, 2020/10/19 M7.6 earthquake and 2021/07/29 M8.2 earthquake are plotted as red, magenta and yellow stars. Red and magenta rectangles outline the ensemble of inverse bayesian fault geometry models for the M7.8 and the M7.6 earthquakes, with the postseismic slip of the M7.8 earthquake as the background (Jul 23-Oct 18 2020). Yellow line indicates the coseismic slip for the M8.2 earthquake, retrieved from https://earthquake.usgs.gov/earthquakes/eventpage/ak0219neiszm/finite-fault. In image (b), red and orange dashed lines correspond to the 0.5m slip contours for the M7.8 coseismic fault slip estimated by this research and Ye et al. (2021). The first 3-month aftershocks following the M7.8 event are plotted as gray dots.

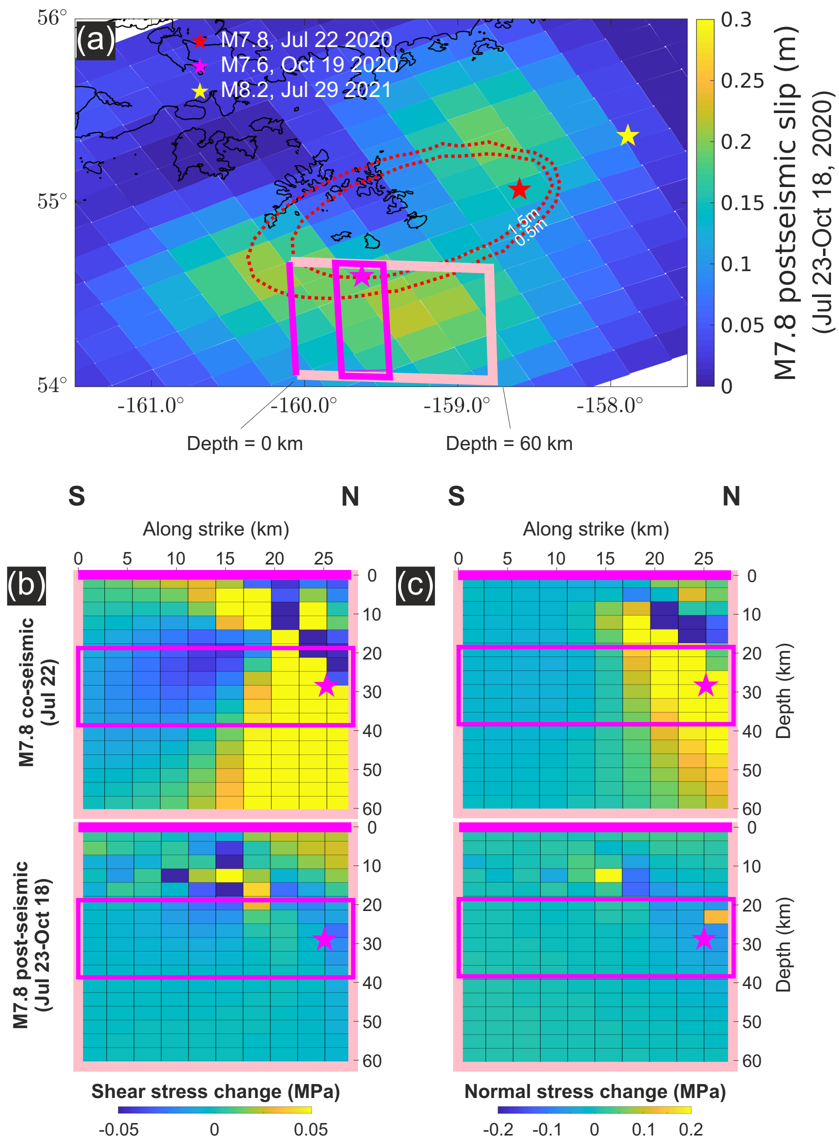

Figure 6: Coulomb stress change on the M7.6 fault model. In image (a), the red dashed contour lines indicate 0.5m and 1.5m of the M7.8 coseismic slip, and the background color indicate the postseismic slip of the M7.8 earthquake. The magenta rectangle outlines the ensemble of inverse Bayesian fault geometry model for the M7.6 earthquake, and the pink rectangle is the extended model from the surface (depth=0) to depth=60 km. Images (b)-(c) present the stress change on the extended geometry of the M7.6 fault model, caused by the M7.8 coseismic and postseismic slip distributions shown in (a).

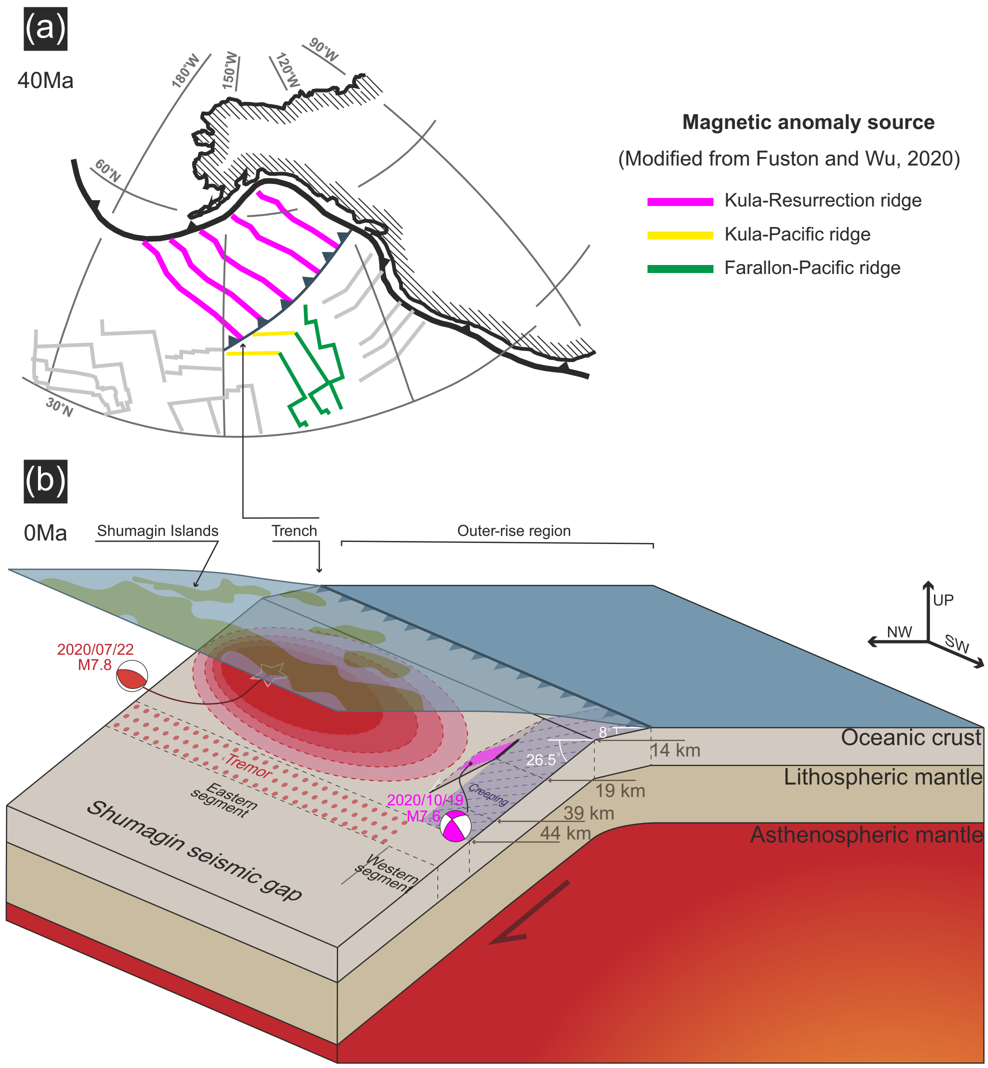

Figure 7: Conceptual model of the main subduction zone characteristics where the megathrust earthquake occurs in the plate interface and the triggered strike-slip earthquake tears the incoming oceanic lithosphere. Image (a) shows the slab plate tectonic reconstruction of western North America at 40Ma, modified from Fuston and Wu (2020). The magenta lines indicated the magnetic anomalies caused by the Kula-Resurrection ridge, which was subducted beneath the Aleutian Islands in the present days. Yellow and green lines present the magnetic anomalies caused by Kula-Pacific ridge and Farallon-Pacific ridge. This Pacific-Farallon-Kula triple junction moved to the north with the subducting Pacific plate and is located in the outer-rise region close to Shumagin Islands now.

Figure 7 (continued): In image (b), the red shaded region is the rupture area at 14-44 km depth caused by the Jul 22 2020 M7.8 event. The magenta shaded region is the rupture area caused by the Oct 19 2020 M7.6 event. The latter fault might be a reactivated pre-existing fault before subducting, caused by the seafloor spreading of Kula-Resurrection ridge, as shown in image (a).

References

Abercrombie, R.E., Antolik, M., Ekström, G., 2003. The June 2000 Mw 7.9 earthquakes south of Sumatra: Deformation in the India-Australia Plate. Journal of Geophysical Research: Solid Earth 108, ESE 6–1–ESE 6–16. doi:10.1029/2001JB000674.

Beavan, J., Wang, X., Holden, C., Wilson, K., Power, W., Prasetya, G., Bevis, M., Kautoke, R., 2010. Near-simultaneous great earthquakes at Tongan megathrust and outer rise in September 2009. Nature 466, 959–963. doi:10.1038/nature09292.

Blewitt, G., Hammond, W.C., Kreemer, C., 2018. Harnessing the gps data explosion for interdisciplinary science. Eos 99, 1–2. doi:10.1029/2018EO104623.

Brown, J.R., Prejean, S.G., Beroza, G.C., Gomberg, J.S., Haeussler, P.J., 2013. Deep low-frequency earthquakes in tectonic tremor along the Alaska-Aleutian subduction zone. Journal of Geophysical Research: Solid Earth 118, 1079–1090. doi:10.1029/2012JB009459.

Brune, J.N., 1970. Tectonic stress and the spectra of seismic shear waves from earthquakes. Journal of Geophysical Research (1896-1977) 75, 4997–5009. doi:10.1029/JB075i026p04997.

Crowell, B.W., Melgar, D., 2020. Slipping the Shumagin Gap: A Kinematic Coseismic and Early Afterslip Model of the M_w 7.8 Simeonof Island, Alaska, Earthquake. Geophysical Research Letters 47, e2020GL090308. doi:10.1029/2020GL090308.

Davies, J., Sykes, L., House, L., Jacob, K., 1981. Shumagin Seismic Gap, Alaska Peninsula: History of great earthquakes, tectonic setting, and evidence for high seismic potential. Journal of Geophysical Research 86, 3821. doi:10.1029/JB086iB05p03821.

Dieterich, J.H., 1978. Preseismic fault slip and earthquake prediction. Journal of Geophysical Research: Solid Earth 83, 3940–3948. doi:10.1029/JB083IB08P03940.

Drooff, C., Freymueller, J.T., 2021. New Constraints on Slip Deficit on the Aleutian Megathrust and Inflation at Mt. Veniaminof, Alaska From Repeat GPS Measurements. Geophysical Research Letters 48, e2020GL091787. doi:10.1029/2020GL091787.

Duputel, Z., Kanamori, H., Tsai, V.C., Rivera, L., Meng, L., Ampuero, J.P., Stock, J.M., 2012. The 2012 Sumatra great earthquake sequence. Earth and Planetary Science Letters 351-352, 247–257. doi:10.1016/j.epsl.2012.07.017.

Elliott, J.R., Jolivet, R., Gonzalez, P.J., Avouac, J.P., Hollingsworth, J., Searle, M.P., Stevens, V.L., 2016. Himalayan megathrust geometry and relation to topography revealed by the Gorkha earthquake. Nature Geoscience 9, 174–180. doi:10.1038/ngeo2623.

Estabrook, C.H., Jacob, K.H., Sykes, L.R., 1994. Body wave and surface wave analysis of large and great earthquakes along the eastern Aleutian Arc, 1923-1993: implications for future events. Journal of Geophysical Research 99, 643–654. doi:10.1029/93jb03124.

Fournier, T.J., Freymueller, J.T., 2007. Transition from locked to creeping subduction in the Shumagin region, Alaska. Geophysical Research Letters 34, L06303. doi:10.1029/2006GL029073.

Freymueller, J.T., Suleimani, E.N., Nicolsky, D.J., 2021. Constraints on the Slip Distribution of the 1938 M_w 8.3 Alaska Peninsula Earthquake From Tsunami Modeling. Geophysical Research Letters 48, e2021GL092812. doi:10.1029/2021GL092812.

Fukahata, Y., Wright, T.J., 2008. A non-linear geodetic data inversion using ABIC for slip distribution on a fault with an unknown dip angle. Geophysical Journal International 173, 353–364. doi:10.1111/j.1365-246X.2007.03713.x.

Fukuda, J., Johnson, K.M., 2008. A fully Bayesian inversion for spatial distribution of fault slip with objective smoothing. Bulletin of the Seismological Society of America 98, 1128–1146. doi:10.1785/0120070194.

Funning, G.J., Garcia, A., 2019. A systematic study of earthquake detectability using Sentinel-1 Interferometric Wide-Swath data. Geophysical Journal International 216, 332–349. doi:10.1093/gji/ggy426.

Fuston, S., Wu, J., 2020. Raising the Resurrection plate from an unfolded-slab plate tectonic reconstruction of northwestern North America since early Cenozoic time. GSA Bulletin doi:10.1130/b35677.1.

Hansen, R.A., Ratchkovski, N.A., 2001. The Kodiak Island, Alaska M_w 7 Earthquake of 6 December 1999. Seismological Research Letters 72, 22–32. doi:10.1785/gssrl.72.1.22.

Hayes, G.P., Moore, G.L., Portner, D.E., Hearne, M., Flamme, H., Furtney, M., Smoczyk, G.M., 2018. Slab2, a comprehensive subduction zone geometry model. Science 362, 58–61. doi:10.1126/science.aat4723.

Hearn, E.H., 2003. What can GPS data tell us about the dynamics of post-seismic deformation? Geophysical Journal International 155, 753–777. doi:10.1111/j.1365-246X.2003.02030.x.

Herman, M.W., Furlong, K.P., 2021. Triggering an unexpected earthquake in an uncoupled subduction zone. Science Advances 7, eabf7590. doi:10.1126/sciadv.abf7590.

Hubbard, J., Almeida, R., Foster, A., Sapkota, S.N., Bürgi, P., Tapponnier, P., 2016. Structural segmentation controlled the 2015 M_w 7.8 Gorkha earthquake rupture in Nepal. Geology 44, 639–642. doi:10.1130/G38077.1.

Jiang, Y., González, P.J., 2020. Bayesian Inversion of Wrapped Satellite Interferometric Phase to Estimate Fault and Volcano Surface Ground Deformation Models. Journal of Geophysical Research: Solid Earth 125. doi:10.1029/2019JB018313.

Kanamori, H., 1971. Seismological evidence for a lithospheric normal faulting — the Sanriku earthquake of 1933. Physics of the Earth and Planetary Interiors 4, 289–300. doi:10.1016/0031-9201(71)90013-6.

Ke, C.Y., McLaskey, G.C., Kammer, D.S., 2020. The Earthquake Arrest Zone. Geophysical Journal International doi:10.1093/gji/ggaa386.

King, G.C.P., Stein, R.S., Lin, J., 1994. Static stress changes and the triggering of earthquakes. Bulletin of the Seismological Society of America 84, 935–953.

Kohli, A.H., Goldsby, D.L., Hirth, G., Tullis, T., 2011. Flash weakening of serpentinite at near-seismic slip rates. Journal of Geophysical Research 116, B03202. doi:10.1029/2010JB007833.

Krabbenhoeft, A., von Huene, R., Miller, J.J., Lange, D., Vera, F., 2018. Strike-slip 23 January 2018 MW 7.9 Gulf of Alaska rare intraplate earthquake: Complex rupture of a fracture zone system. Scientific Reports 8, 13706. doi:10.1038/s41598-018-32071-4.

Lange, D., Tilmann, F., Rietbrock, A., Collings, R., Natawidjaja, D.H., Suwargadi, B.W., Barton, P., Henstock, T., Ryberg, T., 2010. The Fine Structure of the Subducted Investigator Fracture Zone in Western Sumatra as Seen by Local Seismicity. Earth and Planetary Science Letters 298, 47–56. doi:10.1016/j.epsl.2010.07.020.

Lay, T., 2015. The surge of great earthquakes from 2004 to 2014. Earth and Planetary Science Letters 409, 133–146. doi:10.1016/j.epsl.2014.10.047.

Lay, T., 2021. Alaska EarthScope and Beyond, Feb 8: Thorne Lay and Carl Tape - MSU MediaSpace. URL: https://mediaspace.msu.edu/media/Alaska+EarthScope+and+Beyond%2C+Feb+8A+Thorne+Lay+and+Carl+Tape/1_kmi3a07i.

Li, J., Shillington, D.J., Bécel, A., Nedimović, M.R., Webb, S.C., Saffer, D.M., Keranen, K.M., Kuehn, H., 2015. Downdip variations in seismic reflection character: Implications for fault structure and seismogenic behavior in the Alaska subduction zone. Journal of Geophysical Research: Solid Earth 120, 7883–7904. doi:10.1002/2015JB012338.

Li, J., Shillington, D.J., Saffer, D.M., Bécel, A., Nedimović, M.R., Kuehn, H., Webb, S.C., Keranen, K.M., Abers, G.A., 2018. Connections between subducted sediment, pore-fluid pressure, and earthquake behavior along the Alaska megathrust. Geology 46, 299–302. doi:10.1130/G39557.1.

Li, Z., Wiens, D., Shen, W., 2020. Crust and Uppermost Mantle Structure of the Alaska Subduction Zone from Joint Inversion of Rayleigh Wave Dispersion and Receiver Functions, in: AGU fall meeting, pp. T055–04.

López, A.M., Okal, E.A., 2006. A seismological reassessment of the source of the 1946 Aleutian 'tsunami' earthquake. Geophysical Journal International 165, 835–849. doi:10.1111/j.1365-246X.2006.02899.x.

Rosen, P.A., Gurrola, E., Sacco, G.F., Zebker, H., 2012. The InSAR scientific computing environment, in: EUSAR 2012; 9th European Conference on Synthetic Aperture Radar, pp. 730–733.

Sendeckyj, G.P., 1970. Elastic inclusion problems in plane elastostatics. International Journal of Solids and Structures 6, 1535–1543. doi:10.1016/0020-7683(70)90062-4.

Seno, T., 2017. Subducted sediment thickness and M_w 9 earthquakes. Journal of Geophysical Research: Solid Earth 122, 470–491. doi:10.1002/2016JB013048.

Shillington, D.J., 2021. Controls on faulting and earthquakes in the Alaska subduction zone. URL: https://balanbbb.corp.csic.es/playback/presentation/2.0/playback.html?meetingId=3ba8aee56e24b4608154f723dc89473b24fb23e8-1616596966813.

Shillington, D.J., Bécel, A., Nedimović, M.R., Kuehn, H., Webb, S.C., Abers, G.A., Keranen, K.M., Li, J., Delescluse, M., Mattei-Salicrup, G.A., 2015. Link between plate fabric, hydration and subduction zone seismicity in Alaska. Nature Geoscience 8, 961–964. doi:10.1038/ngeo2586.

Simoes, M., Avouac, J.P., Cattin, R., Henry, P., 2004. The Sumatra subduction zone: A case for a locked fault zone extending into the mantle. Journal of Geophysical Research: Solid Earth 109, 10402. doi:10.1029/2003JB002958.

Sykes, L.R., 1971. Aftershock zones of great earthquakes, seismicity gaps, and earthquake prediction for Alaska and the Aleutians. Journal of Geophysical Research 76, 8021–8041. doi:10.1029/jb076i032p08021.

Tanioka, Y., Ruff, L., Satake, K., 1995. The great Kurile Earthquake of October 4, 1994 tore the slab. Geophysical Research Letters 22, 1661–1664. doi:10.1029/95GL01656.

Tsai, V.C., Hayes, G.P., Duputel, Z., 2011. Constraints on the long-period moment-dip tradeoff for the Tohoku earthquake. Geophysical Research Letters 38. doi:10.1029/2011GL049129.

Wang, R., Diao, F., Hoechner, A., 2013. SDM - A geodetic inversion code incorporating with layered crust structure and curved fault geometry, in: EGU General Assembly Conference Abstracts, pp. EGU2013–2411.

Wei, S., Helmberger, D., Avouac, J.P., 2013. Modeling the 2012 Wharton basin earthquakes off-Sumatra: Complete lithospheric failure. Journal of Geophysical Research: Solid Earth 118, 3592–3609. doi:10.1002/jgrb.50267.

Weiss, J.R., Qiu, Q., Barbot, S., Wright, T.J., Foster, J.H., Saunders, A., Brooks, B.A., Bevis, M., Kendrick, E., Ericksen, T.L., Avery, J., Smalley, R.S., Cimbaro, S.R., Lenzano, L.E., Barón, J., Báez, J.C., Echalar, A., 2019. Illuminating subduction zone rheological properties in the wake of a giant earthquake. Science Advances 5, 6720–6738. doi:10.1126/sciadv.aax6720.

Weston, J., Ferreira, A.M.G., Funning, G.J., 2014. Joint earthquake source inversions using seismo-geodesy and 3-D earth models. Geophysical Journal International 198, 671–696. doi:10.1093/gji/ggu110.

Ye, L., Lay, T., Kanamori, H., Yamazaki, Y., Cheung, K.F., 2021. The 22 July 2020 M_w 7.8 Shumagin seismic gap earthquake: Partial rupture of a weakly coupled megathrust. Earth and Planetary Science Letters 562, 116879. doi:10.1016/j.epsl.2021.116879.